Journal of Materials Chemistry A

Accepted Manuscript

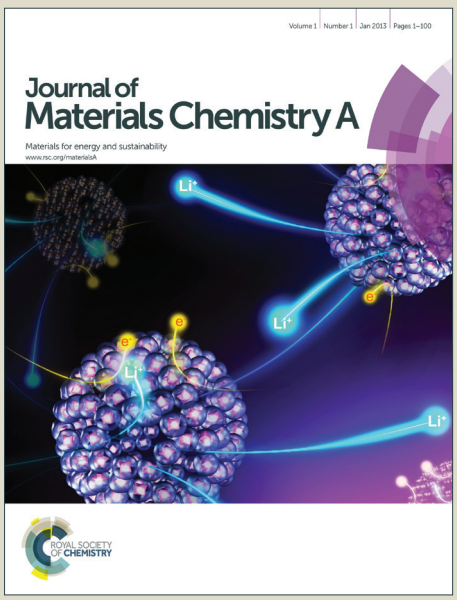

This is an *Accepted Manuscript*, which has been through the Royal Society of Chemistry peer review process and has been accepted for publication.

Accepted Manuscripts are published online shortly after acceptance, before technical editing, formatting and proof reading. Using this free service, authors can make their results available to the community, in citable form, before we publish the edited article. We will replace this *Accepted Manuscript* with the edited and formatted *Advance Article* as soon as it is available.

You can find more information about *Accepted Manuscripts* in the Information for Authors.

Please note that technical editing may introduce minor changes to the text and/or graphics, which may alter content. The journal's standard Terms & Conditions and the Ethical guidelines still apply. In no event shall the Royal Society of Chemistry be held responsible for any errors or omissions in this *Accepted Manuscript* or any consequences arising from the use of any information it contains.

ROYAL SOCIETY OF CHEMISTRY

www.rsc.org/materialsA

Journal Name

ARTICLE TYPE

Cite this: DOI: 10.1039/xxxxxxxxxx

Elucidating the origins of phase transformation hysteresis during electrochemical cycling of Li-Sb electrodes†

Donghee Chang,[a] Hua Huo,[b] Karen E. Johnston,[b] Michel Menetrier,[c,d] Laure Monconduit,[d] Clare P. Grey,[b] and Anton Van der Ven*[a]

Received Date
Accepted Date

DOI: 10.1039/xxxxxxxxxx

www.rsc.org/journalname

We investigate the origins of phase transformation hysteresis in electrodes of Li-ion batteries, focusing on the alloying reaction of Li with Sb. Electrochemical measurements confirm that the reaction path followed during Li insertion into Sb electrodes differs from that followed upon subsequent Li extraction. Results from first-principles calculations and NMR measurements indicate that Li_3Sb is capable of tolerating high Li-vacancy concentrations. An unusually high Li mobility in Li_3Sb facilitates over potentials during charging, which leads to a substantially larger driving force for the nucleation of Sb compared to that of Li_2Sb. The differences in nucleation driving forces arise from a lever effect that favors phases with large changes in Li concentration over phases that are closer in composition along the equilibrium path. These properties provide an explanation for the observed path hysteresis between charge and discharge in the Li-Sb system and likely also play a role in intercalation compounds and other alloying reactions exhibiting similar phase transformation hysteresis.

1 Introduction

Most electrochemically active electrode materials used in Li and Na batteries are intercalation compounds that are capable of accommodating large variations in Li and Na ion concentration.[1–4] Electrochemically viable intercalation compounds, many of them relying on a valence shift of a transition metal ion, maintain the same host crystal structure and undergo only minor variations in lattice parameters as either the Li or Na concentration is varied. Electrochemical cycling can therefore occur without substantial degradation. Although ideal in many ways for electrochemical energy storage applications, intercalation compounds nevertheless have a limited capacity as measured by the amount of Li or Na that can be removed and reinserted into the compound.

Alternative solid-state reaction mechanisms that differ qualitatively from intercalation processes are also possible. An important class includes displacement and conversion reactions whereby the extrusion and subsequent precipitation of a transition metal cation occurs simultaneously with the insertion of Li (or Na).[5–8] This mechanism allows for the exploitation of a multi-electron valence shift to achieve very high capacities. Even higher theoretical capacities are possible if the transition metal is eliminated altogether. The Li (or Na) then reacts directly with another element. Li-air and Li-sulfur[9–12] batteries fall in this category, as do electrodes that rely on alloying reactions with Si, Sn, Al and Sb among others.[13–15] The reaction of Li with Si and Sn, for example, can yield compounds with very high Li concentrations (i.e. $Li_{3.75}Si$ and $Li_{4.4}Sn$) making capacities as high as 3579 $mAhg^{-1}$ and 993 $mAhg^{-1}$ theoretically possible.[13,16,17]

While enabling higher capacities, reaction mechanisms that go beyond intercalation often exhibit a large hysteresis in the voltage profile between charge and discharge. A sizable hysteresis leads to unacceptable energy losses during cycling. It is a major impediment to the commercialization of otherwise promising high-capacity electrode chemistries. A fundamental understanding of the factors that cause hysteresis in electrodes undergoing complex solid-state reaction mechanisms is still quite limited.

There are several sources of hysteresis in solid-state electrochemical reactions. One is purely dissipative and emerges from sluggish kinetics on the timescale of the charge and discharge cycle. Slowing the charge and discharge rate can systematically reduce this form of polarization. Hysteresis in the voltage profile will also emerge if the reaction follows a different path during

[a] Materials Department, University of California, Santa Barbara, 1361A, Engineering II, Santa Barbara, CA, 93106, USA. E-mail: avdv@engineering.ucsb.edu; Tel: +1-805-893-7920
[b] Department of Chemistry, University of Cambridge, Lensfield Road, Cambridge, CB2 1EW, UK
[c] CNRS, Universite de Bordeaux, ICMCB - 87 Avenue Schweitzer, Pessac F33600, France
[d] Institut Charles Gerhardt Montpellier-UMR 5253 CNRS, ALISTORE European Research Institute (3104 CNRS), Université Montpellier 2, 34095, Montpellier, France
† Electronic Supplementary Information (ESI) available: [details of NMR measurements]. See DOI: 10.1039/b000000x/

Journal of Materials Chemistry A Accepted Manuscript

discharge compared to that followed during charge.[18–20] The resulting path hysteresis arises due to an asymmetry in competing kinetic mechanisms and becomes more likely as the number of accessible kinetic mechanisms of ion insertion/removal increases.[19] A third source of hysteresis can arise due to mechanical dissipation, either when coherency strains need to be overcome during two-phase coexistence[21] or in the form of plastic deformation, likely an important factor in some alloying reactions undergoing large volume changes.[22]

The aim of this study is to shed light on the causes of phase transformation hysteresis as occurs during the alloying reaction of Sb electrodes in Li-ion batteries. Sb has a specific capacity of 660 $mAhg^{-1}$and undergoes smaller volume changes and fewer phase transformations than Si and Sn when reacting with Li. The electrochemical reaction of Li with Sb electrodes is accompanied by path hysteresis with the discharge voltage profile qualitatively differing in shape from the charge profile. Lithium insertion into Sb electrodes leads first to the formation of Li_2Sb having hexagonal symmetry followed by the formation of Li_3Sb having cubic symmetry.[23,24] Upon Li removal, however, Li_3Sb transforms directly to Sb, bypassing the intermediate hexagonal Li_2Sb phase.[23,24] Hence, the discharge voltage curve should have two plateaus separated by a small step at the Li_2Sb composition, while the charge profile has a single plateau, which is usually about 0.2-0.3 V above the discharge plateaus. The step at Li_2Sb is not always clearly observed, however, the two processes can be clearly resolved by using X-ray diffraction.[24] The hysteresis persists even at low charge and discharge rates. In spite of this path hysteresis, the charge and discharge profiles as well as the capacity does not change much over many cycles[25] in contrast to bulk Si and Sn electrodes, which can show large irreversible capacity losses.[13,26]

With the aim of elucidating the origin of the path hysteresis exhibited by the alloying reaction of Li with Sb, we combine first-principles calculations with electrochemical and NMR studies to establish a range of crystallographic, electronic, thermodynamic and kinetic properties of the three phases that form during the electrochemical reaction of Li with Sb. Based on these property predictions we argue that path hysteresis in Sb electrodes arises from an asymmetry in the competition between Li diffusion rates and driving forces for nucleation. These triggers are likely common to many other electrode chemistries that suffer from path hysteresis.

2 Methods

Computational Methods

First-principles electronic structure calculations were performed using density functional theory (DFT) within the generalized gradient approximation as parameterized by Perdew-Burke-Ernzerhof (PBE).[27] We used the Vienna Ab initio simulation package (VASP) plane wave pseudo-potential code[28,29] with the projector augmented wave method (PAW) to describe the interactions between valence and core electrons.[30,31] An energy cutoff of 400 eV was used. We used a Γ-point centered 12×12×12 k-point mesh for the primitive cell of Li_3Sb, a 6×6×6 k-point mesh for the unit cell of Li_2Sb and a 12×12×4 mesh for the unit cell of Sb. The energy cutoff and k-point grid used in this study were sufficient to converge the calculated energies to within 1 meV per formula unit. The k-point meshes for the supercells of these structures were chosen to yield a similar k-point density in reciprocal space. Ionic positions and the lattice parameters of each structure were fully relaxed.

To study off stoichiometry at room temperature (as opposed to 0 K), we also performed a statistical mechanical study of the thermodynamic properties using cluster expansion Hamiltonians[32,33] and Monte Carlo simulations. We used the CASM software package[34–36] to construct the cluster expansions and parameterize their coefficients to first-principles total energy calculations as well as to perform Monte Carlo simulations.

Lithium migration mechanisms and barriers were determined using the climbing image nudged-elastic-band method,[37] as implemented in VASP. For each phase, a large supercell was used, allowing all atoms to relax while holding the lattice parameters and volume of the supercell fixed.

To calculate electronic densities of state and band structures of A7 Sb, hexagonal Li_2Sb and cubic Li_3Sb we used the HSE06 hybrid functional.[38]

Electrode Preparation

All electrodes for *ex situ* ^{7}Li NMR studies were prepared as self-supporting films using carboxymethyl cellulose (CMC) (degree of substitution DS = 0.7, and average molecular weight M_w = 250,000 g mol^{-1}, Aldrich) as a binder with two conductive additives: (i) vapor-grown carbon fibers (VGCF, diameter 100-200 nm and length 10-20 μm, Brunauer-Emmett-Teller (BET) surface areas 15 m^2g^{-1}, SHOWA DENKO) and (ii) carbon black Y50A (CB, BET primary particle size 20-60 nm, primary aggregate size 100 nm, surface area 70 m^2g^{-1}). The Sb powder (350 mesh, 99.5%, Alfa Aesar), CMC and additives were manually grounded in a mortar and pestle with a weight ratio of 70:12:9:9% (Sb:CMC:Y50A:VGCF). The mixture was then mixed with deionised water in a silicon nitride vial containing three 9.5 mm diameter silicon nitride balls. A Fritsch Pulverisette 7 was used to mill the mixture at 500 rpm for 1 hour. The slurry was tape cast onto 22 μm thick copper foil at 150 μm thickness. The electrodes were then dried for 12 hours at room temperature and 1 hour at 100 °C under vacuum. To prepare electrodes for *in situ* NMR, the slurry was cast onto one end of a pre-weighed strip of copper mesh, leaving the uncoated side to serve as the battery lead.

Electrochemical Tests

All *ex situ* NMR measurements were completed in 2032-type coin cells. Sb electrodes were cycled against Li metal with 1 M $LiPF_6$ dissolved in a 1:1 volumetric mixture of ethylene carbonate (EC) and dimethyl carbonate (DMC). Each cell was assembled inside an argon-filled glovebox. Electrochemical curves were recorded on an Arbin Instrument at room temperature under galvanostatic conditions. After electrochemical cycling, the cells were disassembled in a glovebox, where the active materials were extracted and packed into zirconia rotors for NMR analysis. Each sample

Journal of Materials Chemistry A Accepted Manuscript

This journal is © The Royal Society of Chemistry [year]

therefore remains under an inert environment.

For all *in situ* NMR studies a flexible battery design was used, where the positive electrode was prepared using the method described above.[39] The negative electrode was constructed by pressing lithium metal onto copper mesh, leaving bare copper mesh at one end to act as the battery lead. A VSP cycler (Bio-Logic) was used for cycling the *in situ* cells.

Solid-State NMR Spectroscopy

***Ex situ* NMR Data** All room temperature ^{6,7}Li static and magic-angle spinning (MAS) NMR spectra were acquired using a Bruker Avance 400 MHz spectrometer, equipped with a wide-bore 9.4 T magnet using Larmor frequencies of 58.88 MHz and 155.51 MHz for ^{6}Li ($I = 1$) and ^{7}Li ($I = 3/2$), respectively. The powdered samples were packed into conventional 2.5 mm zirconia rotors and a MAS rate of 30 kHz was employed. A rotor-synchronized Echo-MAS sequence was used (90°-τ-180°-τ). Two-dimensional magnetization exchange ^{6,7}Li NMR spectra were acquired using the sequence $(\pi/2)$-τ_1-$(\pi/2)$-τ_m-$(\pi/2)$-τ_2-acq, where τ_1 and τ_2 represent interpulse delays and τ_m is the mixing time. A range of mixing times were tested, including 0.1, 10, 50 and 200 ms.

***In situ* NMR Data** All static ^{7}Li NMR spectra were acquired using a Tecmag 300 MHz spectrometer, equipped with a wide-bore 7 T magnet using a Larmor frequency of 116.64 MHz. Single pulse experiments with a recycle delay of 1 s were employed using a static probe equipped with a 1 cm coil. To improve the signal-to-noise ratio of the ^{7}Li NMR spectra, low-pass filters (50 MHz) were used to filter any high-frequency noise arising from the cycler. All ^{6,7}Li chemical shifts were referenced to 1 M LiCl (aq) at $\delta_{iso} = 0$ ppm.

3 Results

3.1 Crystallography

There are three distinct phases that can coexist when Li alloys with Sb. The first is pure Sb, prototype A7, which belongs to space group R$\bar{3}$m (No.166).[40] The crystal structure consists of puckered layers and is shown in Fig. 1a. The second phase is hexagonal Li_2Sb belonging to space group P$\bar{6}$2c (No.190)[41] and is shown in Fig. 1b. The last phase is Li_3Sb which has cubic symmetry and belongs to space group Fm$\bar{3}$m (No.225).[40,42,43] Since A7 Sb, hexagonal Li_2Sb and cubic Li_3Sb are distinct phases that can tolerate some degree of off-stoichiometry, we will refer to them with the Greek letters α, β and γ respectively.

α-Sb, β-Li_2Sb and γ-Li_3Sb can each be described as the stacking of either triangular Sb layers or a combination of triangular and honeycomb Sb layers. Following convention, we denote stacking sequences of triangular layers with the letters A, B and C. To emphasize that these layers are triangular lattices, we add a subscript t such that the stacking in fcc, for example, would be denoted by $A_tB_tC_t$. There are also several ways of stacking a honeycomb network, which can also be denoted by the letters A, B and C. For a honeycomb layer, we add the subscript h. In describing the crystallographic relationships between α-Sb, β-Li_2Sb and γ-Li_3Sb, we will also need to distinguish between layers that have been rotated by 30 degrees around an axis perpendicular to the layer. We label these layers with a prime, e.g. $A_{t'}$.

The crystal structure of pure α-Sb is similar to the fcc lattice except that every other close-packed (111) layer is off-centered. Fig. 1c illustrates the α-Sb crystal structure as represented by layers of triangular lattices. The triangular lattices have an $A_tB_tC_t$ stacking sequence as in fcc, but with non-uniform spacing between pairs of planes. The off-centering of alternating layers allows the Sb of one close-packed plane to form three short bonds with neighboring Sb of the other close-packed plane (Fig. 1a).

The crystal structure of hexagonal β-Li_2Sb is also layered in the sense that the Sb sublattice can be described as consisting of two-dimensional honeycomb layers, A_h, interleaved by two-dimensional triangular lattices, $A_{t'}$. The Sb-Sb nearest neighbor distance within the $A_{t'}$ layers of β-Li_2Sb is substantially larger than that in the triangular layers of pure Sb as they reside above and below the centers of the honeycomb rings of the adjacent A_h layers. The Sb sublattice is identical to the omega phase of elemental metals such as Ti and Zr and their suboxides.[44,45] The Li ions occupy two symmetrically distinct interstitial sites within this Sb sublattice. The first is a five-fold coordinated square pyramidal site (6h Wyckoff position), while the second is a four fold coordinated tetrahedral site (6g Wyckoff position).

The Sb sublattice of γ-Li_3Sb forms a perfect fcc lattice, which is a stacking of close-packed triangular lattices, i.e. $A_tB_tC_t$. The Li ions occupy all the octahedral and tetrahedral interstitial sites of the fcc Sb sublattice.

Although several crystallographic pathways linking α-Sb to the Sb sublattice of the β-Li_2Sb phase can be identified, one is especially straightforward. It relies on the splitting of each triangular lattice of Sb into a honeycomb layer and a new triangular lattice that is rotated by 30 degrees and has a much larger nearest neighbor distance between Sb. An A_t layer of pure α-Sb, for example, can split into a A_h honeycomb layer and a $A_{t'}$ layer, as illustrated in Fig. 1c. The Sb atoms of A_t that ultimately form the $A_{t'}$ triangular lattice form a $\sqrt{3} \times \sqrt{3}$ supercell in the original A_t layer. If every triangular layer splits in this manner, an intermediate crystal is formed with $A_hA_{t'}B_hB_{t'}C_hC_{t'}$ stacking, as illustrated in Fig. 1c. This intermediate crystal must be sheared to obtain the $A_hA_{t'}A_hA_{t'}A_hA_{t'}$ of the Sb sub lattice in β-Li_2Sb, as shown in Fig. 1c.

A similar mechanism connects the Sb sublattice of β-Li_2Sb with that of γ-Li_3Sb. The collapse of a honeycomb network A_h with a triangular lattice $A_{t'}$ forms a triangular lattice A_t. The collapse of pairs of A_h and $A_{t'}$ must also be accompanied by a shear to take the resulting $A_tA_tA_t$ stacking to an fcc $A_tB_tC_t$ stacking characterizing the Sb sublattice of γ-Li_3Sb.

In view of the crystallographic similarities between the three phases, the possibility exists that the two-phase reactions between any pair of them could occur coherently. An important metric to analyze this possibility is the transformation strain required to deform one crystal into the other. If the transformation strain is small, the two-phase reaction may proceed coherently without incurring large coherency strain energy penalties. The transformation strain can be defined using the starting phase as the reference. The Green-Lagrange strain tensor, E, is related to the

Journal of Materials Chemistry A Accepted Manuscript

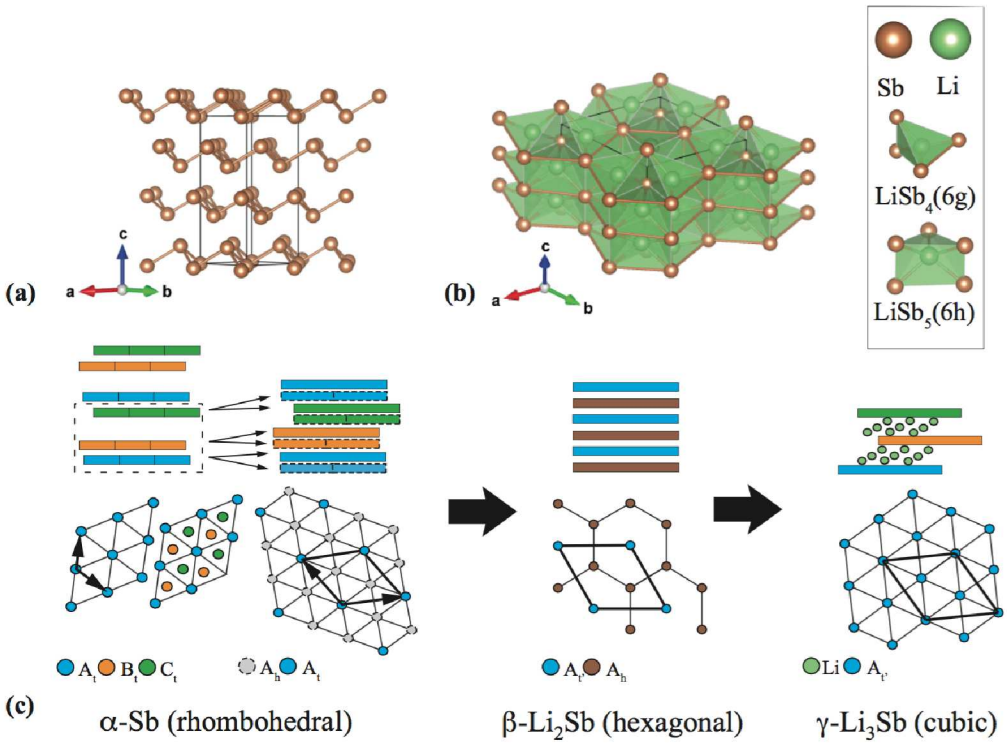

Fig. 1 Crystal structures of (a) pure α-Sb ($R\bar{3}m$, prototype A7) and (b) hexagonal β-Li_2Sb ($P\bar{6}2c$). (c) Schematic illustrations of structural transformations from α-Sb to β-Li_2Sb and from β-Li_2Sb to γ-Li_3Sb. A_t,B_t, and C_t represent triangular lattices and A_h represents a honeycomb network. $A_{t'}$ represents a triangular lattice rotated by 30 degrees.

deformation gradient $\hat{F}$ according to

$$E = \frac{\hat{F}^{+}\hat{F} - I}{2} \quad (1)$$

where, for homogeneous strain, the 3×3 deformation gradient matrix $\hat{F}$ relates the lattice vectors of the transformed crystal $\mathbf{a}'$, $\mathbf{b}'$ and $\mathbf{c}'$ to the lattice vectors of the original crystal $\mathbf{a}$, $\mathbf{b}$ and $\mathbf{c}$ according to $\mathbf{a}' = \hat{F}\mathbf{a}$. $\hat{F}^{+}$ corresponds to the transpose of $\hat{F}$.

In general, large misfit strains between the original crystal structure and the new crystal structure will incur large strain energy costs when the two phases coexist coherently. If this strain energy is larger than the cost of forming an incoherent interface, the transformation will occur reconstructively. As is to be expected for alloying reactions, the volume changes in the Li-Sb system are very large. Transforming from α-Sb to β-Li_2Sb results in a volume change of close to 90%, while the addition of Li to β-Li_2Sb to form γ-Li_3Sb results in a further increase of about 35% relative to the Sb volume. Large volume changes by themselves, though, do not necessarily result in strain energy penalties. There are special anisotropic transformation strains in which particular crystallographic planes do not undergo a strain as the original crystal transforms into the new crystal. The transformation can then proceed coherently in the absence of coherency strains if the interface separating the growing phase from the original phase within an electrode particle is parallel to these strain invariant planes. The requirement for the existence of a strain invariant plane is that one eigenvalue of E is equal to 0, one eigenvalue is greater than 0 and one eigenvalue is less than 0.[46]

Table 1 The eigenvalues of the transformation strains for various crystallographic transformation paths using experimentally measured lattice parameters

Transformation path	λ_1	λ_2	λ_3
α-Sb → β-Li_2Sb	-0.0416	0.0669	1.3652
α-Sb → γ-Li_3Sb	-0.1031	0.0817	2.4883
β-Li_2Sb → γ-Li_3Sb	-0.2224	0.0130	0.7493
β-Li_2Sb → α-Sb	-0.3660	-0.0590	0.0453
γ-Li_3Sb → β-Li_2Sb	-0.2999	-0.0127	0.4007
γ-Li_3Sb → α-Sb	-0.4163	-0.0702	0.1299

The eigenvalues of the transformation strains (Eq. 1), assuming the crystallographic transformation paths described above and using experimentally measured lattice parameters,[40,41] are listed in Table 1. The transformation strains are very large as is clear by the large eigenvalues. However, they all show at least one positive and one negative eigenvalue as well as an eigenvalue close to zero. Nevertheless, the eigenvalues close to zero are still sizable and thus none of the transformation strains exhibit a strict strain invariant plane. If any of these transformations occur coherently, they will be accompanied by coherency strain. We point out though that the transformations that most closely approach the conditions for a strain invariant plane are between Li_2Sb and Li_3Sb.

Journal of Materials Chemistry A Accepted Manuscript

This journal is © The Royal Society of Chemistry [year]

3.2 First-Principles Results

Electronic structure

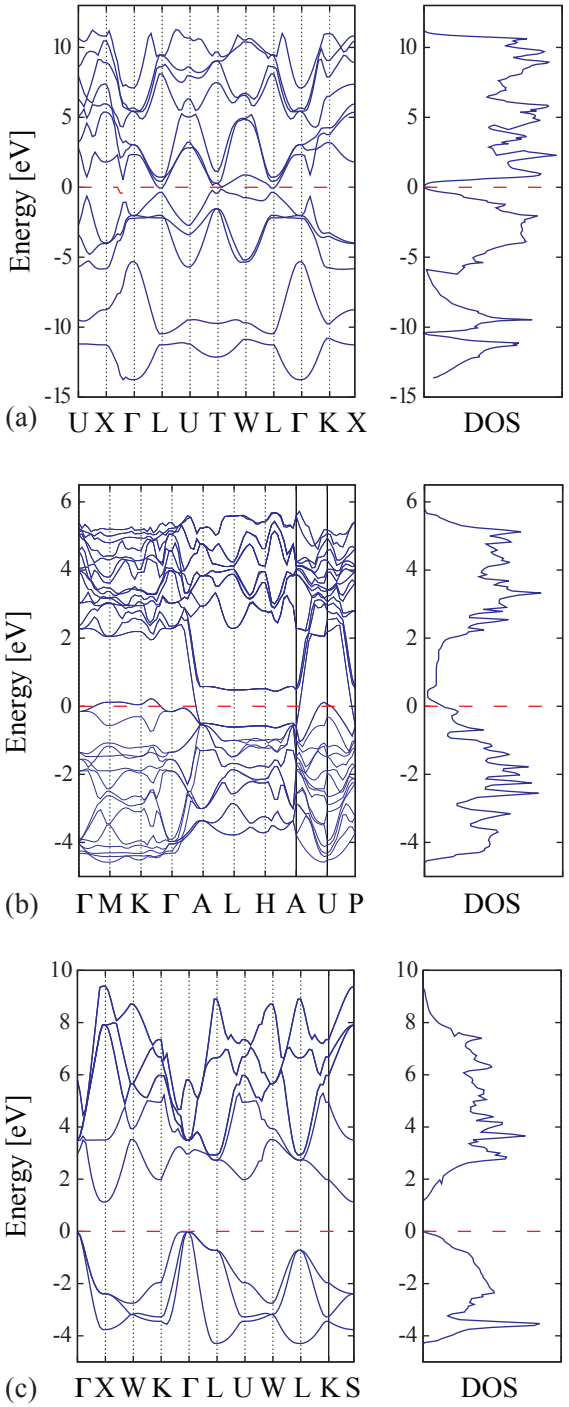

Fig. 2 Calculated electronic density of states and band structures of (a) α-Sb (rhombohedral unit cell), (b) β-Li_2Sb (hexagonal unitcell), and (c) γ-Li_3Sb using the HSE screened hybrid functional. The Fermi level is set to zero.

The electrodes of an electrochemical cell should exhibit some degree of electronic conductivity such that electrons can reach the electrode/electrolyte interface where the electrochemical reactions occur. We used both DFT-PBE as well as HSE06[38] to calculate the electronic density of states and band structure of α-Sb, β-Li_2Sb and γ-Li_3Sb. The density of states and band structure as calculated with HSE06 are shown in Fig. 2. Both α-Sb and γ-Li_3Sb are predicted to be semi-conductors having band gaps of approximately 0.05 and 1.1 eV respectively. β-Li_2Sb is predicted to be metallic, but with the Fermi level close to a minimum in the density of states.

Lithium removal from γ-Li_3Sb lowers the Fermi level into the valence band resulting in the creation of holes. The density of states rises sharply when decreasing the Fermi level away from the valence band maximum. This suggests that the holes, created upon Li removal, will likely form itinerant states that are mobile, very quickly making γ-$Li_{3-y}Sb$ electronically conducting. The band gap of α-Sb is predicted to be very small. As described above, the A7 form of α-Sb can be derived from perfect fcc Sb by reducing the distance between alternating pairs of close packed planes, thereby lowering the symmetry of the crystal and doubling the size of the primitive unit cell. Perfect fcc Sb is predicted with HSE06 not to have a band gap. The band gap emerges as alternating pairs of (111) planes are shifted off center to form the A7 crystal structure (Fig. 3). The addition of interstitial Li to the Sb host should shift the Fermi level into the conduction band. Again, the density of states increases very rapidly when moving into the conduction band, suggesting that electrons donated by inserted Li are likely to be delocalized and itinerant due to the strong dispersion of the conduction bands.

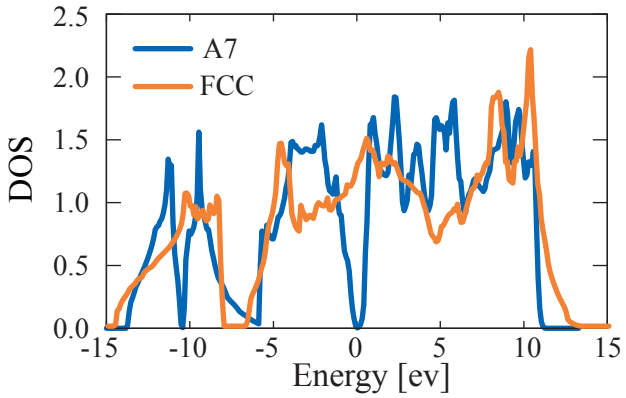

Fig. 3 Density of states of the A7 form of α-Sb (blue) and the perfect fcc form of Sb (orange). The A7 form of α-Sb is similar to the fcc lattice with the exception that every other close-packed(111) layer is off-centered.

Thermodynamic properties

An electrode material that undergoes path hysteresis will pass through metastable states for at least some portion of the charge and discharge process. While α-Sb, β-Li_2Sb and γ-Li_3Sb are line compounds their crystal structures suggest that they can tolerate some degree of off-stoichiometry, either by introducing interstitial Li in α-Sb, or by creating Li vacancies in β-Li_2Sb and γ-Li_3Sb. To determine the accessibility of these metastable off-stoichiometric compositions, we calculated the free energies of dilute α-Sb, β-Li_2Sb and γ-Li_3Sb using a cluster expansion approach.

Journal of Materials Chemistry A Accepted Manuscript

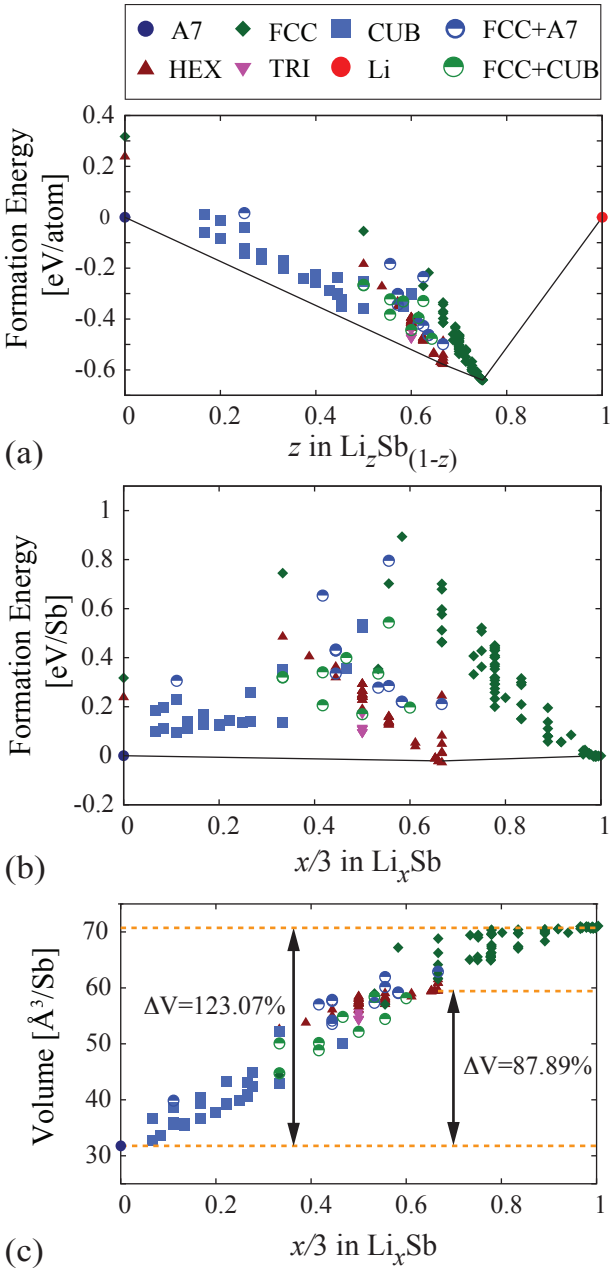

Fig. 4 Formation energies of different configurations calculated from first-principles (a) per atom using α-Sb and pure Li as a reference (b) per Sb using γ-Li_3Sb and α-Sb as a reference. The energies of the ground states are connected with a black line forming a convex hull. (c) Volume per Sb for all calculated structures between α-Sb and γ-Li_3Sb. The changes in the volume of the ground state phases is shown with a dotted orange line.

Throughout the remainder of the text, we will work with different composition variables depending on the context. In some contexts it is convenient to track the number of Li, N_{Li}, normalized by the number of Sb, N_{Sb}, a quantity we will denote with $x = N_{Li}/N_{Sb}$. This composition variable appears in the chemical formula Li_xSb. In other contexts, it is convenient to work with an atomic fraction, which we define as $z = N_{Li}/(N_{Li}+N_{Sb})$. In terms of z, the chemical formula of the alloy is then $Li_zSb_{(1-z)}$. We will also denote off-stoichiometric forms of α-Sb, β-Li_2Sb and γ-Li_3Sb as $Li_\delta Sb$, $Li_{2-\varepsilon}Sb$ and $Li_{3-\zeta}Sb$ respectively, where δ refers to a dilute Li concentration and ε and ζ refer to dilute vacancy concentrations (all normalized by the number of Sb).

As a first step in parameterizing cluster expansion Hamiltonians for each compound, we enumerated symmetrically distinct Li-vacancy orderings over the interstitial sites of α-Sb and over the Li sites of hexagonal $Li_{2-\varepsilon}Sb$ and cubic $Li_{3-\zeta}Sb$. The Li-vacancy orderings were enumerated within symmetrically distinct supercells of the primitive unit cells of the parent compounds. We calculated the total energies of these configurations with DFT-PBE as implemented in VASP. Fig. 4a shows the resulting formation energies, defined as

$$\Delta E(z) = E(z) - zE_{Li} - (1-z)E_{Sb} \qquad (2)$$

where, $E(z)$ is the DFT energy of a particular configuration in a supercell having an atomic fraction z. The energy $E(z)$ is normalized by the total number of atoms within that supercell ($N_{Li}+N_{Sb}$). E_{Li} and E_{Sb} are DFT energies per atom of bcc Li and α-Sb respectively.

Fig. 4a shows that hexagonal β-Li_2Sb, and cubic γ-Li_3Sb are predicted to be stable intermediate compounds in the Li-Sb binary. Interestingly, configurations having very dilute vacancy concentrations over the octahedral sites of γ-$Li_{3-\zeta}Sb$ are also predicted to reside on the convex hull (e.g. $Li_{2.96}$ and $Li_{2.98}Sb$). Moreover, a large number of configurations with dilute concentrations of lithium vacancies in hexagonal β-Li_2Sb and cubic γ-Li_3Sb have formation energies close to the convex hull.

Fig. 4b shows formation energies calculated relative to α-Sb and γ-Li_3Sb and plotted versus Li concentration $x/3$. The energies of each structure in this plot are normalized by the number of Sb atoms. This figure more clearly illustrates the stability of the different metastable structures relative to the three ground states α-Sb, β-Li_2Sb and γ-Li_3Sb. The volumes of the different structures are also shown in Fig. 4c as a function of $x/3$.

The introduction of large vacancy concentrations in β-Li_2Sb and γ-Li_3Sb often causes the original structure to relax to very different final structures. We have been able to distinguish between several categories of crystal structures that emerge when relaxing β-Li_2Sb and γ-Li_3Sb upon removal of Li. The energies of these structures are denoted by different symbols in Fig. 4. The green diamonds (FCC) correspond to energies of structures in which the Sb sublattice of $Li_{3-\zeta}Sb$ maintains its fcc sublattice as in stoichiometric cubic Li_3Sb. The dark red triangles (HEX) correspond to structures in which the Sb sublattice is that of stoichiometric Li_2Sb. Addition of Li to Sb starting in the A7 crystal structure, even at very dilute Li concentrations, causes the Sb sublattice to adopt a cubic network, as illustrated in Fig. 5a. The

Journal of Materials Chemistry A Accepted Manuscript

This journal is © The Royal Society of Chemistry [year]

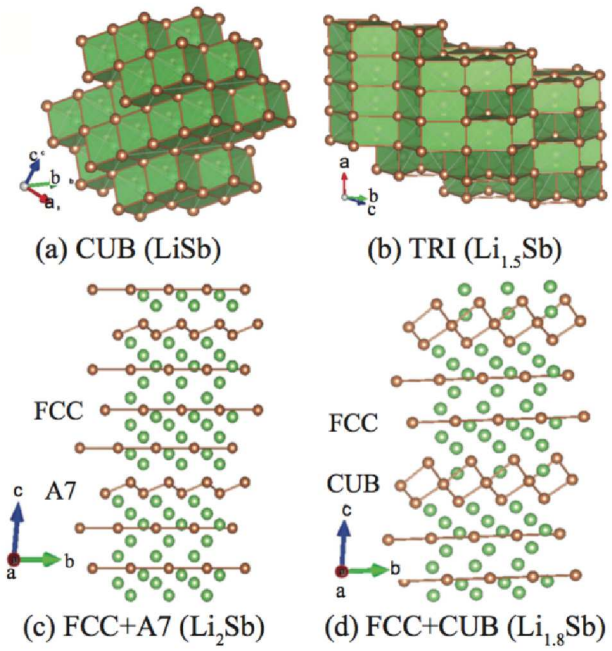

Fig. 5 Examples of relaxed metastable structures upon creation of large vacancy concentrations in hexagonal β-Li_2Sb and cubic γ-Li_3Sb or upon insertion of small lithium concentrations in α-Sb.

energies of these structures are denoted with blue squares (CUB) in Fig. 4. The pink triangles (TRI) having stoichiometry $Li_{1.5}Sb$ in Fig. 4 consist of close-packed triangular Sb sublattices having an $A_tA_tA_t$ stacking sequence (as illustrated in Fig. 5b). The Li occupy a subset of the trigonal prismatic interstitial sites within the Sb sublattice. For Li compositions between LiSb and Li_2Sb, a variety of hybrid structures emerge as shown in Fig. 5c and 5d. The half-blue circles (FCC+A7) in Fig. 4 correspond to the energies of layered structures that have several close packed triangular Sb layers as in fcc interleaved by a puckered Sb layer as in the A7 crystal structure of pure Sb (Fig. 5c). The half-green circles (FCC+CUB) correspond to energies of structures that are also layered, but have Sb triangular lattices interleaved by a layer made up of cubes of Sb as in the cubic structures of dilute Li_xSb (Fig. 5d).

The formation energies of configurations having low vacancy concentrations within hexagonal β-Li_2Sb and cubic γ-Li_3Sb were used to parameterize the expansion coefficients of cluster expansion Hamiltonians.[32,33] Separate cluster expansions were constructed for hexagonal β-$Li_{2-\varepsilon}Sb$ and cubic γ-$Li_{3-\zeta}Sb$. In parameterizing a cluster expansion for cubic γ-$Li_{3-\zeta}Sb$, only configurations that maintained the fcc Sb sublattice after relaxation (FCC in Fig. 4) were used, while in the parameterization of the cluster expansion for the hexagonal phase only configurations that maintained the Sb sublattice of β-Li_2Sb (HEX in Fig. 4) were used.

The cluster expansions were subjected to grand canonical Monte Carlo simulations to predict the dependence of the Li chemical potential on Li concentration within each compound. This dependence was then integrated to calculate the Gibbs free energy, g (normalized by the total number of atoms) as a function of concentration z. The calculated free energies are shown in

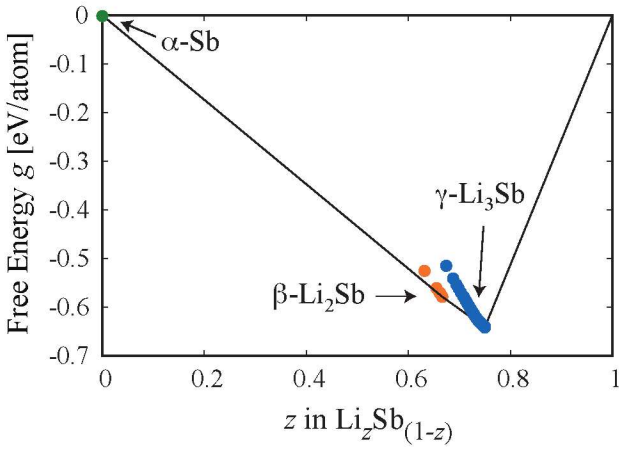

Fig. 6 The calculated free energies of β-$Li_{2-\varepsilon}Sb$ and γ-$Li_{3-\zeta}Sb$ at 300 K plotted as a function of atomic fraction z in Li_zSb_{1-z}.

Fig. 6.[47]

The voltage of an electrochemical cell using metallic Li as the anode is related to the Li chemical potentials according to

$$V(z) = -(\mu_{Li}(z) - \mu^o_{Li})/e \qquad (3)$$

where, $\mu_{Li}(z)$ is the Li chemical potential in Li_zSb_{1-z} and μ^o_{Li} is the Li chemical potential of metallic Li. The chemical potentials in Eq. 3 are in units of eV and e corresponds to the charge of an electron.

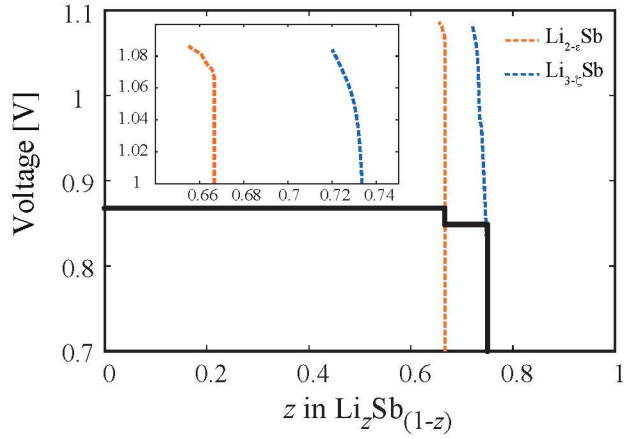

Fig. 7 Equilibrium voltage profile (solid black line) and metastable voltage profiles for $Li_{2-\varepsilon}Sb$ (orange dashed line) and $Li_{3-\zeta}Sb$ (blue dashed line).

Fig. 7 shows the calculated equilibrium voltage curve as a function of Li concentration. A small step at the composition of β-Li_2Sb (z=0.66) separates two plateaus corresponding to two-phase reactions between α-Sb and β-Li_2Sb and between β-Li_2Sb and γ-Li_3Sb respectively. The step height is approximately 40 mV. Fig. 7 also shows metastable voltage profiles for β-$Li_{2-\varepsilon}Sb$ and γ-$Li_{3-\zeta}Sb$. Cubic γ-$Li_{3-\zeta}Sb$ can reach high vacancy concentrations ($\zeta \sim 0.5$) with a 0.2V overpotential relative to the equilibrium γ-Li_3Sb to β-Li_2Sb voltage plateau.

Journal of Materials Chemistry A Accepted Manuscript

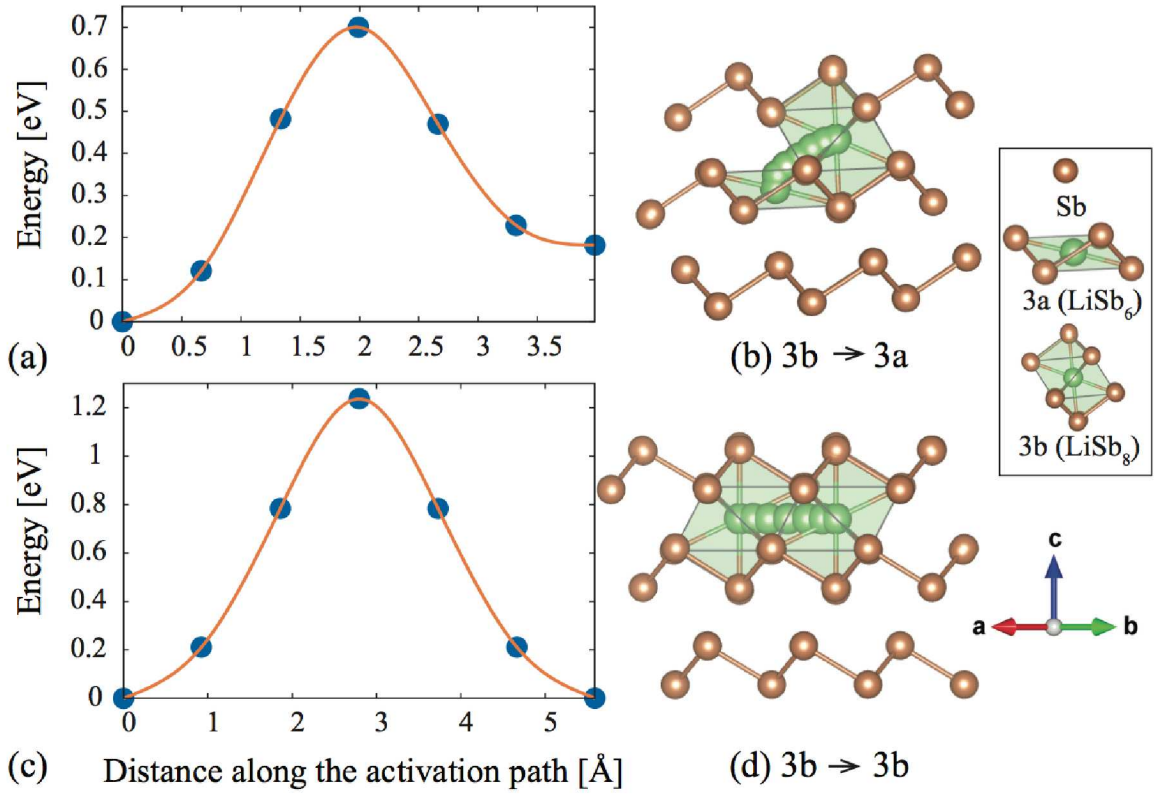

Fig. 8 Migration barriers and paths for Li hops in α-Sb at dilute Li concentrations. (a) Barrier and (b) hop path for a Li hop from an eightfold coordinated site to an adjacent compressed octahedral site. (c) Barrier and (d) hop path for a Li hop in a basal plane from an eightfold coordinated site to an adjacent eightfold coordinated site.

Kinetic properties

Li diffusion within the three stable compounds is an important property as it determines the rates with which the electrode can be charged and discharged and is likely to play a role in the selection of kinetic pathways. A key quantity in assessing the mobility of Li ions is the migration barrier of individual hops. Diffusion in most electrode materials for Li-ion batteries occurs at non-dilute concentrations and can be quite complex due to the dependence of migration barriers and hop mechanisms on the local concentration and the varying degrees of disorder among lithium and vacancies.[48] A treatment of non-dilute diffusion requires kinetic Monte Carlo approaches combined with cluster expansion techniques, for example, to describe the dependence of atomic hop barriers on the local degree of Li-vacancy ordering.[34,49–51] Since α-Sb, hexagonal β-$Li_{2-\varepsilon}Sb$ and cubic γ-$Li_{3-\zeta}Sb$ are essentially line compounds, we need only consider diffusion in the presence of dilute concentrations of diffusion mediating defects such as Li interstitials or Li vacancies. The diffusion coefficient in these dilute limits is directly proportional to individual atomic hop frequencies,[48] which can be approximated with transition state theory.[52]

In α-Sb, the relevant diffusion process is the migration of an isolated interstitial Li from one site to an adjacent interstitial site, while in hexagonal β-$Li_{2-\varepsilon}Sb$ and cubic γ-$Li_{3-\zeta}Sb$ atomic diffusion is mediated through the migration of isolated vacancies and possibly divacancies between adjacent sites of the Li sublattices of the compounds. Using the nudged elastic band method as implemented in VASP, we calculated the migration barriers for elementary hops in α-Sb, β-Li_2Sb and γ-Li_3Sb.

For nudged elastic band calculations of isolated interstitial Li hops in α-Sb, we used a $3\times3\times2$ supercell of the hexagonal unit cell of A7 Sb (lattice constant a,b = 13.14 Å, c = 22.99 Å), while for Li hops into isolated vacancies in β-Li_2Sb we used a $2\times2\times2$ supercell of the hexagonal unit cell (lattice constant a = 13.10 Å, b,c = 15.89 Å). Nudged elastic band calculations for Li hops into isolated vacancies and divacancies in cubic γ-Li_3Sb were performed with a $3\times3\times3$ supercell of the primitive cell of cubic Li_3Sb (lattice constant a = 13.93 Å).

At dilute Li concentrations, individual Li ions can occupy two distinct interstitial sites in A7 Sb: an eightfold coordinated site (3b), and a compressed octahedral site (3a). The eightfold 3b site is more stable than the compressed octahedral 3a site by ~200 meV. Li can hop between adjacent sites, either by performing a curved hop by passing through an intermediate tetrahedral site or by following a direct hop as illustrated in Fig. 8b and 8d. The calculated migration barriers shown in Fig. 8a and 8c, are high when compared to typical Li migration barriers in electrode materials for Li-ion batteries.[49] The connectivity of these hops forms a three-dimensional network, such that Li diffusion will be three dimensional.

There are two symmetrically distinct Li sites in hexagonal Li_2Sb, a tetrahedral site (6g) and a square pyramidal site (6h).

Journal of Materials Chemistry A Accepted Manuscript

This journal is © The Royal Society of Chemistry [year]

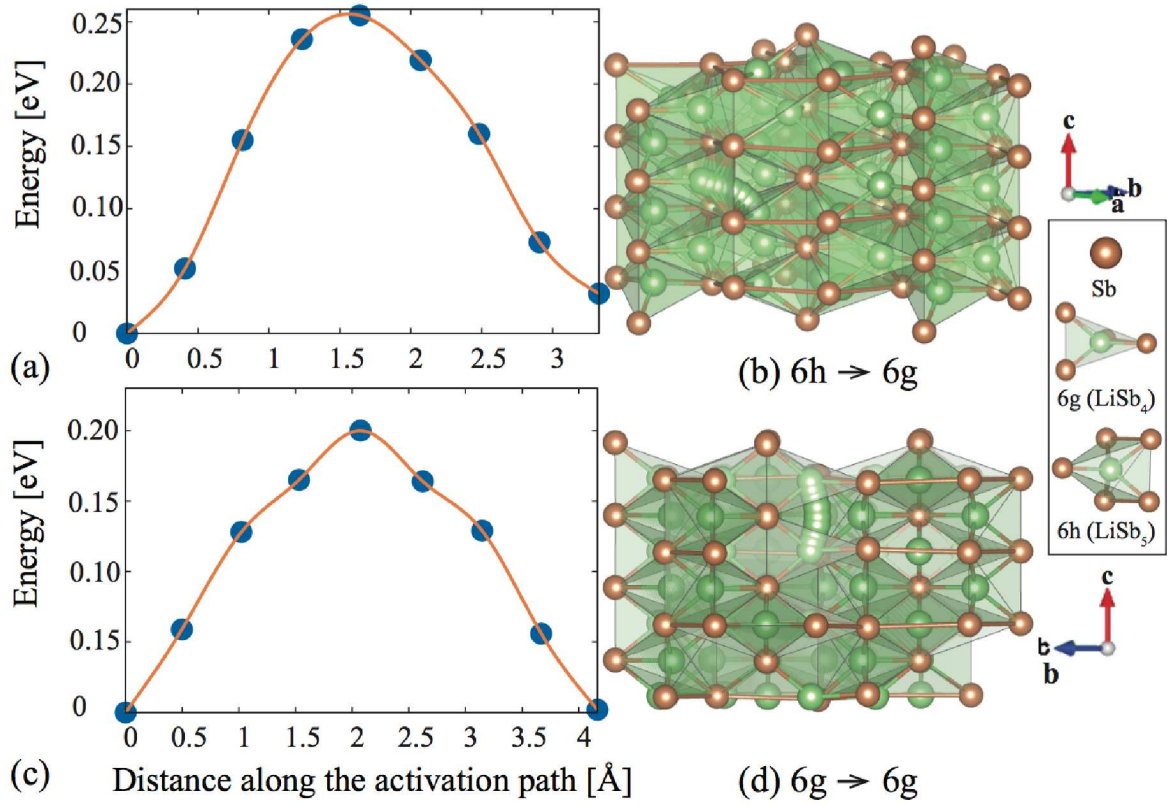

Fig. 9 Migration barriers and paths for Li hops in hexagonal β-Li_2Sb. (a) Barrier and (b) hop path for a Li hop from a square pyramidal site to an adjacent vacant tetrahedral site. (c) Barrier and (d) hop path for a Li hop between neighboring tetrahedral sites parallel to the **c** axis.

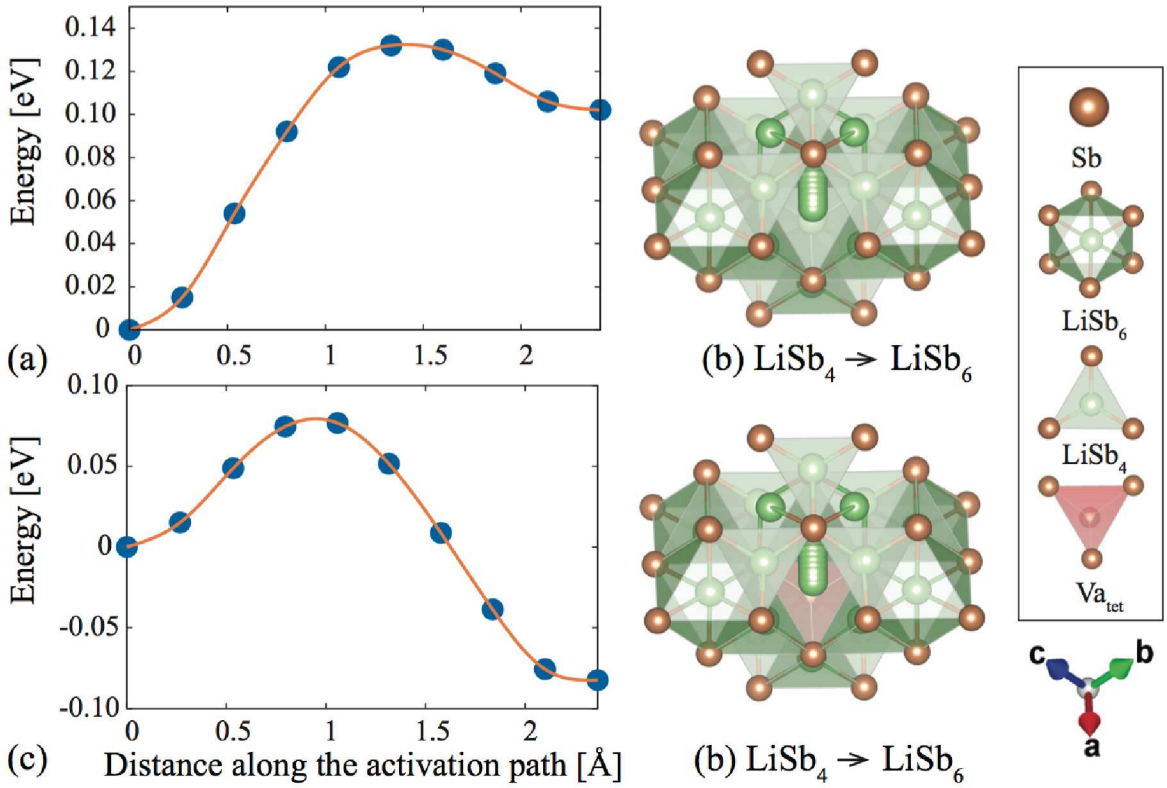

Fig. 10 Migration barriers and paths for Li hops in cubic γ-Li_3Sb having an fcc Sb sublattice. (a) Barrier and (b) hop path for Li hop from a tetrahedral site to adjacent vacant octahedral site. (c) Barrier and (d) hop path for a Li hop from a tetrahedral site into a vacant octahedral site next to a vacant tetrahedral site (Li hops into a divacancy).

Journal of Materials Chemistry A Accepted Manuscript

An isolated vacancy prefers to reside in the 6g tetrahedral site. The energy increases by ~40 meV when the vacancy moves from the tetrahedral site to the 6h square pyramidal site. Fig. 9a shows the energy as a Li ion migrates from the square pyramidal site to a neighboring vacant tetrahedral site. Li can also hop between neighboring tetrahedral sites parallel to the **c** axis and the energy for this hop is shown in Fig. 9c. The migration barriers for both hops are of the order of 200-250 meV. Hops between neighboring tetrahedral sites or neighboring square pyramidal sites parallel to the basal plane of the hexagonal unit cell are also possible, however, the barriers for these hops are of the order of 1 eV and are therefore unlikely to contribute much to macroscopic Li diffusion. The collection of the symmetrically equivalent nearest neighbor hops with low barriers forms a three dimensional network.

The Li ions of cubic Li_3Sb fill both the tetrahedral and octahedral interstitial sites of the fcc Sb sublattice. An isolated vacancy prefers to reside on the octahedral site. The energy of the crystal increases by 100 meV when the vacancy moves from the octahedral site to the tetrahedral site. The energy along the migration path as a Li atom hops from a tetrahedral site to an octahedral site is shown in Fig. 10a. The energy barrier is less than 150 meV, a very small value. A similar migration barrier was recently predicted by Baggetto et al[25] for Li_3Sb. The calculated free energy for γ-$Li_{3-\zeta}Sb$ shown in Fig. 6 suggests that Li_3Sb can tolerate off stoichiometry and that vacancy clusters may be prominent.[48] We therefore also considered Li hops into a divacancy. Fig. 10c shows the energy as a Li hops from a tetrahedral site into a vacant octahedral site next to a vacant tetrahedral site. While isolated vacancies in Li_3Sb prefer to reside on octahedral sites, when an octahedral vacancy is next to a tetrahedral vacancy, the energy of the crystal actually decreases when a tetrahedral Li hops into the octahedral site, thereby forming two tetrahedral vacancies. The barrier for this hop, as for the single vacancy hop, is again very low and of the order of 150 meV.

3.3 Electrochemical and NMR Measurements

Ex situ ^{7}Li NMR Studies

A typical discharge/charge curve obtained for Sb/Li, using a cycle rate of C/30 (full capacity, in this case, equating to 3 Li per Sb in 30 hours), is shown in Fig. 11a. A series of samples were extracted from batteries stopped after discharging/charging to different states, as indicated by the red dots on the voltage-capacity profile. Samples are denoted as Li_xSb, where x denotes the Li content calculated from the discharging/charging time. The Li content of the sample is calculated assuming 100% coulombic efficiency. The ^{7}Li MAS and static NMR spectra obtained for each sample are shown in Fig. 11b and 11c, respectively. In each MAS spectrum, a sharp and a broad resonance are observed at -1 ppm and 0 ppm. These are assigned to the electrolyte and solid electrolyte interphase (SEI), respectively.

Two resonances appear in a 1:1 ratio at 40 and -17 ppm in the MAS spectrum for the sample obtained at the beginning of discharge, corresponding to composition $Li_{0.2}Sb$. The intensities of both resonances increase until a maximum is reached after 15 hours of discharge, corresponding to a composition of $Li_{1.5}Sb$. Their intensities then decrease (see the $Li_{2.5}Sb$ spectrum) until they disappear at the end of the first discharge ($Li_{3.2}Sb$). These two resonances are absent from the following charge process but reappear during the second discharge. The apparent Li:Sb ratio of greater than 3.0 is ascribed to SEI formation and the presence of Li in non-Sb containing SEI components. This behavior is consistent with the observation of Li_2Sb via *in situ* XRD studies.[24] Hence, the resonances at 40 and -17 ppm are tentatively assigned to the Li sites in Li_2Sb; this structure contains two Li sites with multiplicities of 1:1 consistent with the observed intensity ratio of 1:1.

Two weak resonances are also observed at 3.8 and -8.5 ppm in the spectrum of $Li_{0.75}Sb$, acquired during the first discharge. The intensity of the resonance at -8.5 ppm increases upon further lithiation, while shifting towards positive chemical shift values: -8.2 ppm at $Li_{1.5}Sb$, -6.7 ppm at $Li_{2.25}Sb$ and -1.4 ppm at the end of discharge, $Li_{3.2}Sb$. During delithiation, this resonance returns to a negative chemical shift value (-8.9 ppm, for $Li_{2.2}Sb$) and reduces in intensity. The resonance at 3.8 ppm, and the series of shifting resonances identified, are tentatively assigned to Li_3Sb and related phases.

To confirm the assignment of the resonances, two-dimensional (2D) ^{7}Li exchange NMR experiments were attempted for samples obtained during the first discharge, specifically those with compositions $Li_{1.5}Sb$ and $Li_{2.25}Sb$. These samples were selected for investigation because they contain all of the ^{7}Li NMR resonances observed during cycling. The 2D method probes magnetization exchange processes between different Li nuclei (via spin diffusion and chemical exchange) for Li species in close spatial proximity, i.e., it is a method used to determine whether resonances belong to the same phase. The ^{7}Li MAS NMR spectrum, and corresponding deconvolution, for $Li_{1.5}Sb$ are shown in Fig. S1a. In addition to the resonances assigned above, a weak resonance at 21 ppm is resolved. 2D ^{7}Li exchange NMR experiments, completed as a function of mixing time for $Li_{1.5}Sb$, contain an asymmetric cross-peak correlating the resonances at 21 and -17 ppm (Fig. S1b), even at 0.1 ms, indicating they belong to the same phase. Clear correlations between the 40 and -17 ppm resonances are seen following a mixing time of 200 ms. Using this, and in conjunction with the information above, the resonances at 40, 21 and -17 ppm are all assigned to Li_2Sb. The resonance at 21 ppm is believed to be due to low concentrations of Li vacancies or interstitials generated during lithiation. The asymmetric cross-peaks are tentatively ascribed to the short spin-lattice relaxation time for the 21 ppm resonance.[53] The presence of a non-stoichiometric Li_2Sb phase is consistent with the calculated free energy of Li_2Sb, which is very shallow and remains close to the common tangent as the Li concentration is reduced (Fig. 6).

Cross-peaks were also observed for the resonances at 3.8 and -8.2 ppm in the 200 ms 2D experiment, consistent with their assignment to the same phase (Li_3Sb). ^{6,7}Li 2D NMR spectra of $Li_{2.25}Sb$ (see the Supporting Information for more details) also shows cross-peaks between the "Li_3Sb" phase peaks at 3.5 and now -6 ppm, along with an additional weak peak at 7 ppm. The relative intensities for the 3.8 ppm peak and the negative peaks are not consistent with the 2:1 multiplicities of the tetrahedral

Journal of Materials Chemistry A Accepted Manuscript

This journal is © The Royal Society of Chemistry [year]

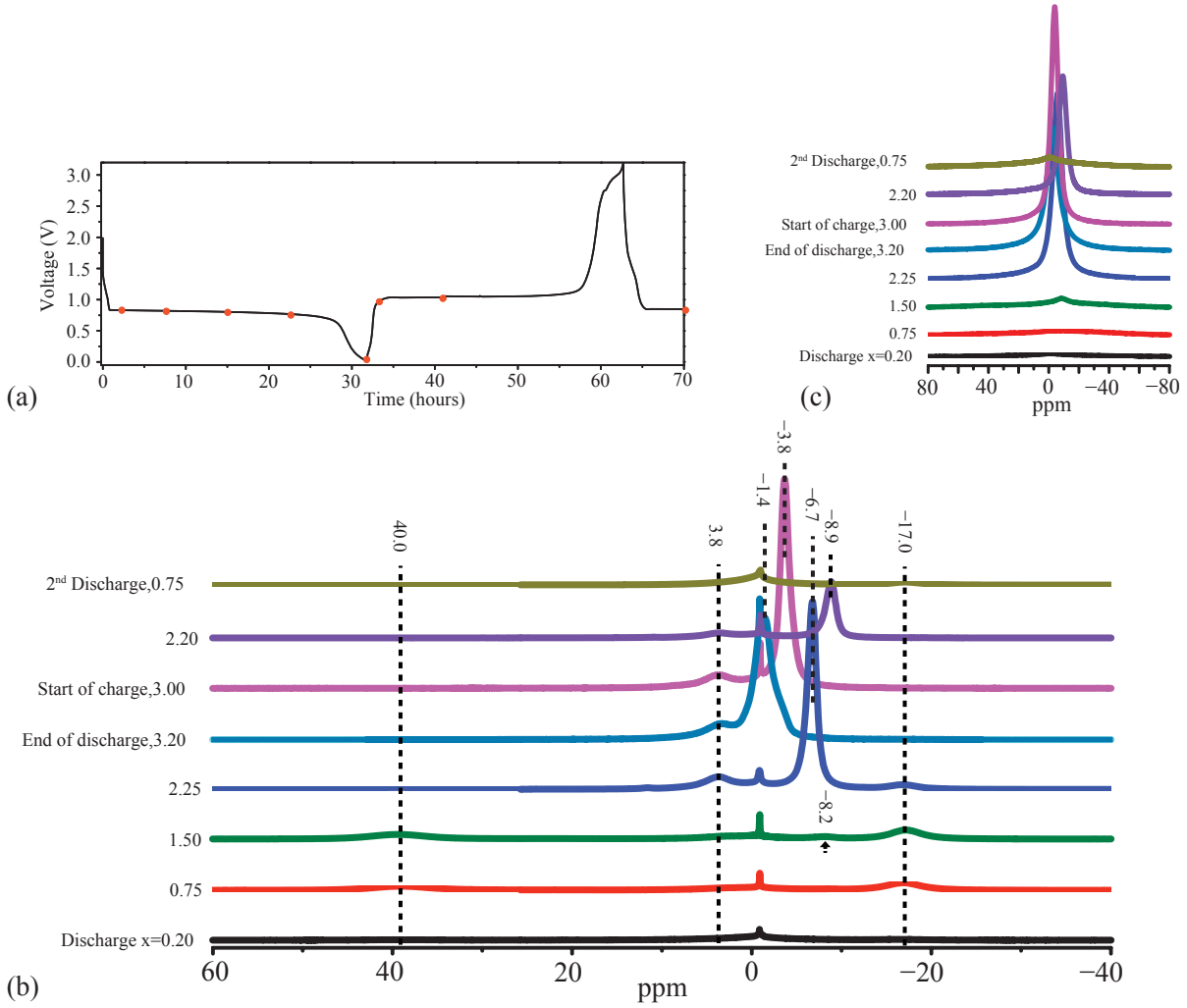

Fig. 11 (a) Electrochemical curve of Li-Sb obtained at a cycle rate of C/30. A series of samples were extracted from batteries stopped after discharging/charging to different states, as indicated by the red dots. The corresponding ^{7}Li static and MAS NMR spectra are shown in (b) and (c), respectively. All spectra were acquired at 9.4 T; MAS spectra were collected with a rate of 30 kHz.

Journal of Materials Chemistry A Accepted Manuscript

and octahedral sites filled by Li in stoichiometric Li_3Sb. We, therefore, ascribe the shifts to the changes in electronic structure (and mobility) induced by non-stoichiometry in Li_3Sb.

The factors that control the ^{6,7}Li shifts in lithium intermetallics are still unclear, many of these compounds being either semiconducting or semi-metals. The larger range of shifts for Li_2Sb than Li_3Sb is, however, consistent with a smaller or zero band gap, although this does not simply explain the observation of the negative resonance. Negative resonances have been observed in the lithium silicide and germanide systems in aromatic silicides ($Li_{12}Si_7$) and in defective $Li_{15}Si_5$ and (stoichiometric and defective) $Li_{15}Ge_4$ [54,55], the latter compounds being very small gap semiconductors.

Static ^{7}Li NMR spectra (Fig. 11c) were acquired to assist in assigning the resonances observed during subsequent *in situ* NMR studies. The resonances observed at 40 and -17 ppm during the MAS study cannot be observed and are presumably buried under the broad baseline. However, the series of shifting resonances observed *ex situ* can be monitored with relative ease via static NMR experiments, as demonstrated in Fig. 11c. This suggests that any changes in chemical shift observed during *in situ* NMR studies will provide valuable insight into the phases formed.

In situ ^{7}Li NMR Studies *In situ* ^{7}Li NMR studies were completed for the first cycle of a Li-Sb cell at a rate of C/30 (Fig. 12). During *in situ* NMR experiments the appearance of resonances corresponding to Li metal and the electrolyte can make it difficult to accurately deconvolute spectra and identify any changes occurring. As a result, "difference spectra" are plotted for the spectra acquired between the two red dots denoted on the voltage-time profile in Fig. 12. Each spectrum was obtained by subtracting the pristine spectrum, i.e., a background spectrum of the cell acquired before electrochemical cycling, from the spectra obtained during cycling.

No obvious changes are observed during the first 10-15 hours of reaction, corresponding to the formation of Li_2Sb. This is consistent with the static *ex situ* NMR studies, where resonances corresponding to Li_2Sb were buried under the baseline. Upon further lithiation, a resonance at approximately 4 ppm appears and gradually increases until the end of discharge. This is in contrast to our *ex situ* NMR study, where resonances with different chemical shifts were observed at different depths of lithiation. During the first 5 hours of charge, the resonance at 4 ppm shifts gradually towards negative chemical shift, reaching approximately -10 ppm. Upon further delithiation, the resonance remains at -10 ppm and the intensity decreases until the end of charge, where it disappears completely.

The resonance observed at 4 ppm during discharge is assigned to stoichiometric Li_3Sb. The resonance that shifts from 4 to -10 ppm during charge in the *in situ* NMR experiment, and from -1.4 to -8.9 ppm during the *ex situ* study is assigned to the delithiated Li_3Sb phase, $Li_{3-\zeta}Sb$. This is in good agreement with the first-principles calculated formation energies and free energy of $Li_{3-\zeta}Sb$, and the suggestion that holes are created upon lithium removal from cubic Li_3Sb (see Fig. 2c). Moreover, this agrees with the suggestion that the structure of Li_3Sb can tolerate some degree of off stoichiometry by introducing Li vacancies.

4 Discussion

Although the charge and discharge of Sb electrodes appears facile and stable over many cycles, it nevertheless exhibits path hysteresis.[23,24] The discharge voltage profile (i.e. during Li insertion) has two plateaus with a small step corresponding to the formation of Li_2Sb, while the charge voltage profile (Li extraction) has a single plateau between Li_3Sb and Sb. The voltage interval in which Li_2Sb is stable relative to Sb and Li_3Sb is very small ($\sim$ 0.04V as predicted from first principles) and may not appear as a sharp step in experimental discharge voltage profiles. Nevertheless, there is a consistent difference of $\sim$ 0.2-0.3 V between charge and discharge with *in situ* XRD indicating the formation of Li_2Sb upon discharge, but its absence during charge.[24] This behavior is confirmed with the *ex situ* NMR measurements performed in this work.

The occurrence of a phase transformation requires some degree of supersaturation, or in electrochemical terms an overpotential relative to the equilibrium potential of two-phase coexistence. It is only then that thermodynamic driving forces for transformation exist. A thermodynamic driving force is defined as a difference between the free energy of the stable phase and the metastable (supersaturated) phase. The grand canonical free energy defined as

$$\phi = \tilde{g} - \mu_{Li} x \tag{4}$$

is the relevant thermodynamic potential when electrochemically controlling the Li chemical potential through the cell voltage (see Eq. 3). In Eq. 4, $\tilde{g}$ is the Gibbs free energy normalized by the number of Sb, N_{Sb}. Figure 13 shows the calculated grand canonical free energies of α-Sb, β-Li_2Sb and γ-Li_3Sb as a function of voltage. Thermodynamic equilibrium at constant voltage (or equivalently at constant μ_{Li}) is determined by the phase with the lowest grand canonical free energy ϕ. Chemical potentials (or voltages) where grand canonical free energies of different phases cross correspond to equilibrium phase transition voltages. It is at these voltages that a plateau emerges in the voltage profile due to a discontinuous change in concentration when going from one phase to the next. As is clear in Figure 13, high voltages (above 0.87 V) stabilize α-Sb, while low voltages below 0.83 stabilize γ-Li_3Sb. The β-Li_2Sb phase is only stable in a narrow voltage window of $\sim$ 0.04 eV. It can be shown that the slopes of the grand canonical free energies in Figure 13 are proportional to the Li concentration x. Since β-Li_2Sb and γ-Li_3Sb have similar Li concentrations, their grand canonical free energy curves, ϕ^β and ϕ^γ, have similar slopes.

The similarities in the slopes of ϕ^β and ϕ^γ as a function of voltage leads to a strong asymmetry in driving forces when transforming from α-Sb to β-Li_2Sb during discharge versus transforming from γ-Li_3Sb to β-Li_2Sb upon charge. During discharge of an Sb electrode, an underpotential (polarization), ΔV, relative to the equilibrium α-Sb $\rightarrow$ β-Li_2Sb voltage of $\sim$ 0.87 V is required to create a driving force, $\Delta\phi^{\alpha\rightarrow\beta} = \phi^\beta - \phi^\alpha$, for the transformation. As is evident in Figure 13, this driving force very rapidly becomes large with increasing underpotential ΔV. While a driving force for a α-Sb to γ-Li_3Sb, $\Delta\phi^{\alpha\rightarrow\gamma}$, also emerges with an underpotential, it is approximately as large as $\Delta\phi^{\alpha\rightarrow\beta}$. In the opposite direction,

Journal of Materials Chemistry A Accepted Manuscript

This journal is © The Royal Society of Chemistry [year]

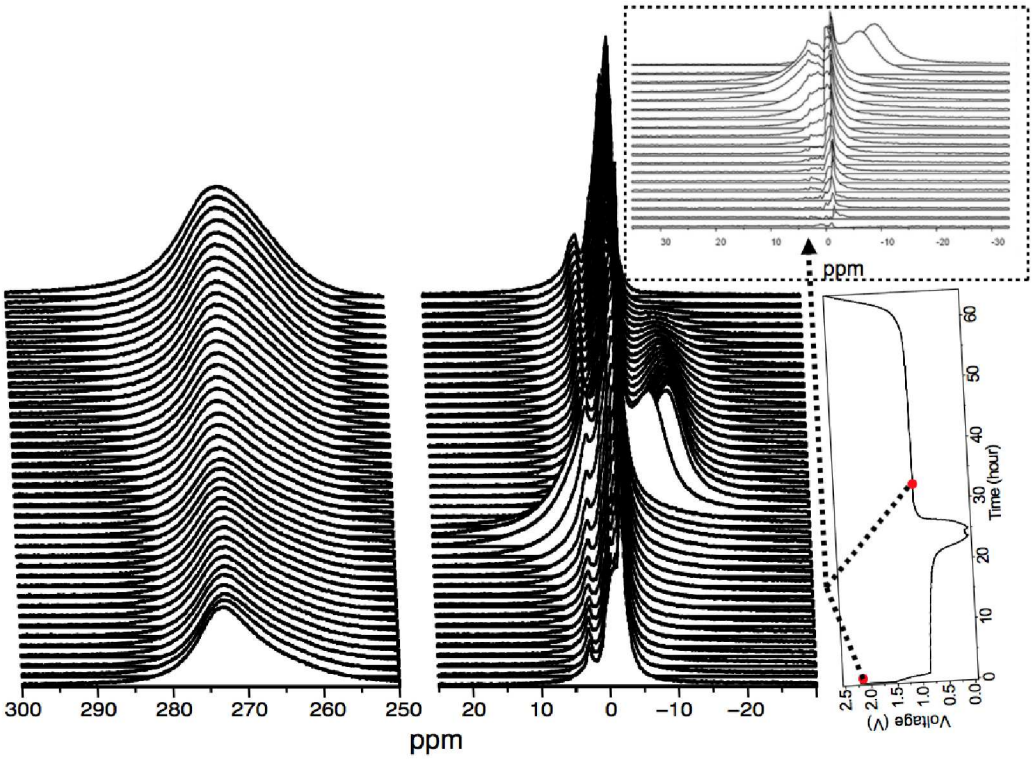

Fig. 12 *In situ* ^{7}Li NMR spectra acquired for the Li-Sb system cycled at a rate of C/30. Signal corresponding to Li metal is shown at 273 ppm. "Difference spectra" are displayed in the inset for the region between the two red dots on the voltage-time curve. "Difference spectra" were obtained by subtracting the background spectrum of the cell obtain before electrochemical cycling from the spectra acquired at subsequent points of them.

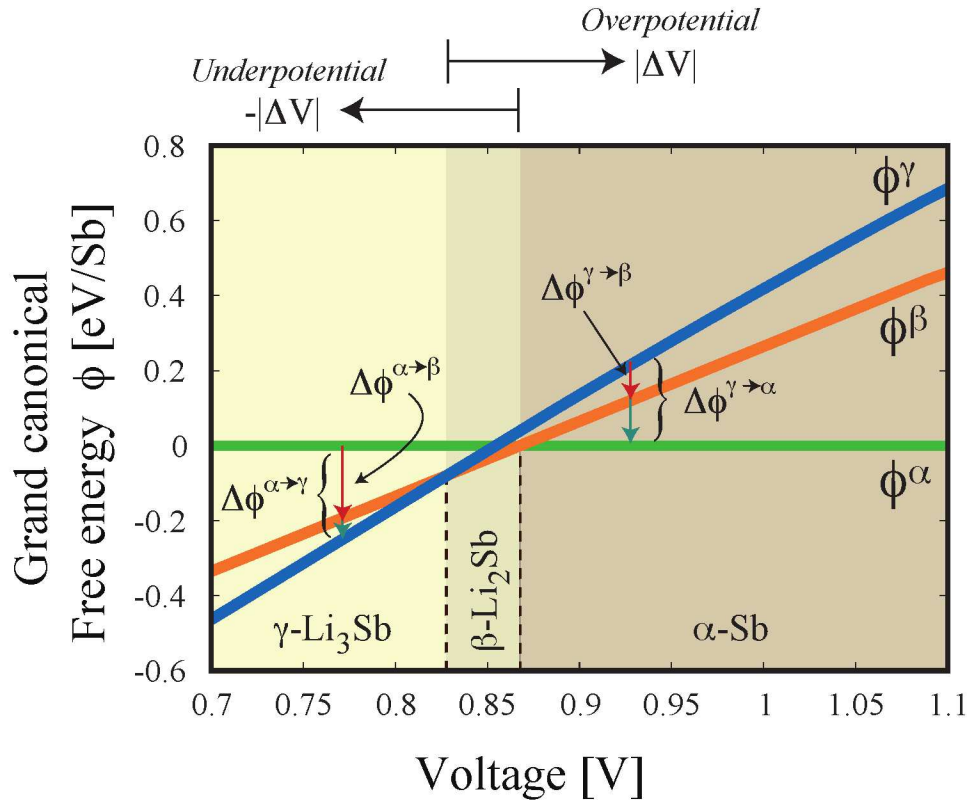

Fig. 13 Grand Canonical Free Energies ϕ for α-Sb, β-Li_2Sb and γ-Li_3Sb as a function of voltage. The grand canonical free energies are normalized by the number of Sb in each phase.

Journal of Materials Chemistry A Accepted Manuscript

when charging γ-Li_3Sb by increasing the voltage above the equilibrium γ - β transition voltage of 0.83 V, the driving force to form β-Li_2Sb, $\Delta\phi^{\gamma\to\beta}$, does not increase markedly with over potential since ϕ^{γ} and ϕ^{β} have similar slopes and run almost parallel to each other. Instead, for overpotentials ΔV larger than $\sim$ 0.02 eV, the driving force for the formation of α-Sb directly from γ-Li_3Sb, $\Delta\phi^{\gamma\to\alpha}$, emerges and very quickly becomes substantially larger than $\Delta\phi^{\gamma\to\beta}$. Figure 13 illustrates a general principle that the driving forces for transformation between phases having similar Li concentrations increases less rapidly with over (under) potential than that between phases having very different concentrations, when controlling the Li chemical potential electrochemically.

The asymmetry is further amplified when considering driving forces for nucleation. Nucleation driving forces and barriers play a key role in phase selection during a phase transformation. The driving force for nucleation is more conveniently represented in Gibbs free energy versus atomic fraction, z, diagrams as schematically illustrated in Figure 14a. The Li chemical potential of a particular phase, α for example, corresponds to the intercept of the tangent to the free energy of α with the z=1 axis. A driving force for nucleation of a new phase β within a preexisting phase α can only emerge if α is supersaturated with respect to its equilibrium solubility limit z^{α} determined by the common tangent to the free energies of α and β as shown schematically in Fig. 14a. A supersaturation in Li concentration ($z > z^{\alpha}$) results in an overpotential $\Delta\mu_{Li}$ relative to the equilibrium Li chemical potential, $\mu_{Li}^{eq.}$, of the $\alpha-\beta$ two-phase coexistence. The overpotential $\Delta\mu_{Li}$ can be represented graphically in a free energy versus concentration plot as illustrated in Fig. 14a. According to Eq. 3, this overpotential in Li chemical potential is equal to -$e\Delta V$, where ΔV is an underpotential in voltage. As shown in Fig. 14a, the driving force for the nucleation of a new phase, β, in a supersaturated phase, α, is equal to the distance between the free energy of β evaluated at the composition of nucleation, z_{nuc}^{β}, and the tangent to the free energy of the supersaturated α phase.[56]. While there are no a priori constraints on the concentration of the nucleus, z_{nuc}^{β}, here we will assume that the new phase nucleates at the same Li chemical potential as that of the parent phase. This is illustrated graphically in Fig. 14a.

Fig. 14b graphically shows the nucleation driving forces for β-Li_2Sb and γ-Li_3Sb in a supersaturated α-Sb phase when an underpotential of 0.1V relative to the equilibrium voltage plateau for the α-Sb to β-Li_2Sb reaction is imposed. As is clear from Fig. 14b, the driving forces $\Delta g_{nuc}^{\alpha\to\beta}$ and $\Delta g_{nuc}^{\alpha\to\gamma}$ to nucleate β-Li_2Sb and γ-Li_3Sb from a supersaturated α-Sb phase upon Li insertion are very similar. Fig. 14c shows the nucleation driving forces for β-Li_2Sb and α-Sb, $\Delta g_{nuc}^{\gamma\to\beta}$ and $\Delta g_{nuc}^{\gamma\to\alpha}$, when an overpotential of 0.1V to extract Li from γ-Li_3Sb is imposed relative to the equilibrium voltage of the γ-Li_3Sb to β-Li_2Sb reaction. In this case, the $\Delta g_{nuc}^{\gamma\to\alpha}$ is substantially larger than $\Delta g_{nuc}^{\gamma\to\beta}$. The much larger difference in concentration between α-Sb and γ-Li_3Sb compared to that between β-Li_2Sb and γ-Li_3Sb results in a lever effect that significantly enhances the nucleation driving force for α-Sb relative to that for β-Li_2Sb.

The lever effect becomes more apparent when the driving force

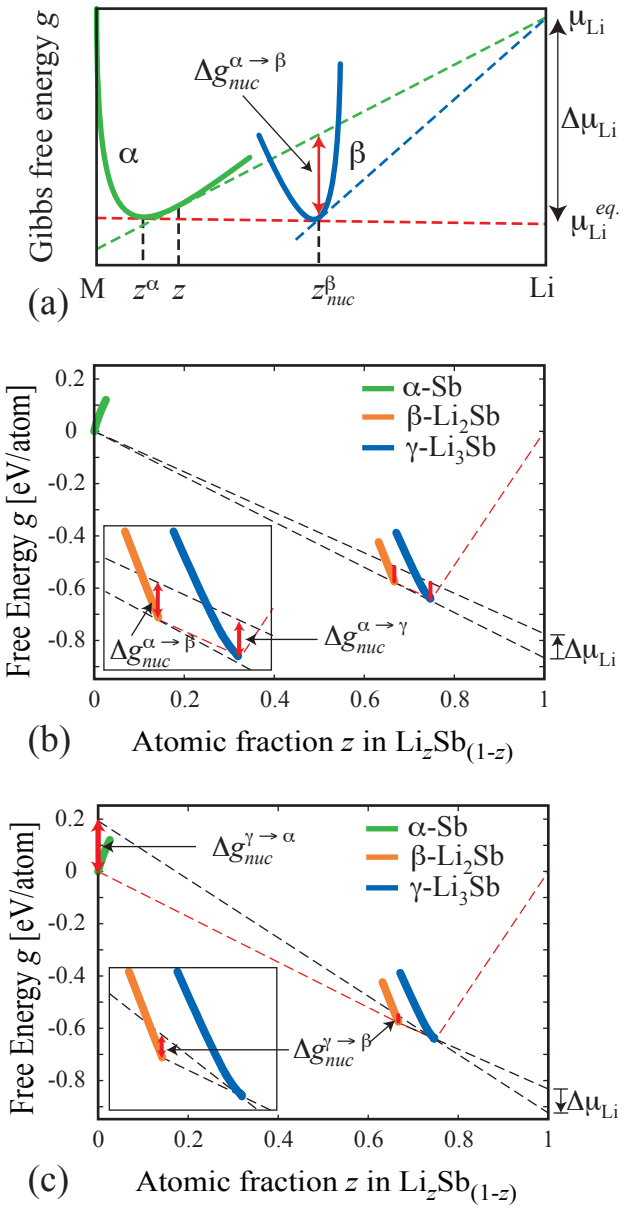

Fig. 14 (a) Schematic illustration of the driving force for the nucleation of a new phase (β) in a supersaturated phase (α). (b) The nucleation driving forces for β-Li_2Sb and γ-Li_3Sb in a supersaturated α-Sb phase when an underpotential of 0.1V relative to the equilibrium voltage plateau for the α-Sb to β-Li_2Sb reaction is imposed. (c) The nucleation driving forces for β-Li_2Sb and α-Sb in a supersaturated γ-Li_3Sb phase when an overpotential of 0.1V to extract Li from γ-Li_3Sb is imposed relative to the equilibrium voltage of the γ-Li_3Sb to β-Li_2Sb reaction.

Journal of Materials Chemistry A Accepted Manuscript

This journal is © The Royal Society of Chemistry [year]

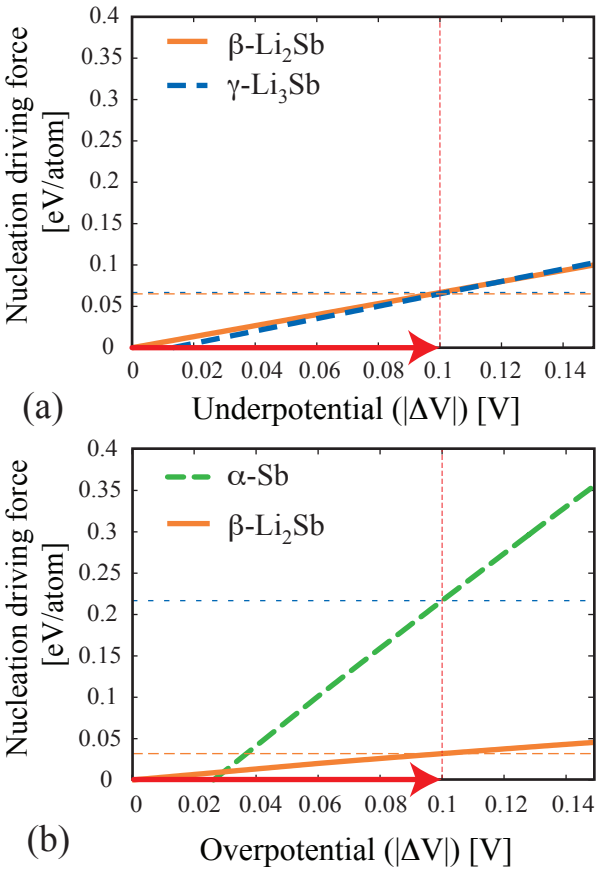

Fig. 15 The nucleation driving forces as a function of over (under) potential. (a) The nucleation driving force for β-Li_2Sb and γ-Li_3Sb when an underpotential to insert Li is applied to α-Sb. (b) The nucleation driving forces for β-Li_2Sb and α-Sb when an overpotential to extract Li from γ-Li_3Sb is applied.

for nucleation is plotted as a function of over (under) potential. Fig. 15a shows the nucleation driving force for β-Li_2Sb and γ-Li_3Sb when an underpotential to insert Li is applied to α-Sb. Since the concentrations of Li_2Sb and Li_3Sb are very close to each other, the nucleation driving forces for both phases are almost identical in value, especially for large over potentials. Consistent with this, weak Li_3Sb resonances are observed even in the $Li_{0.75}Sb$ sample (i.e., during the Sb-Li_2Sb process). The situation is very different when applying an overpotential to extract Li from γ-Li_3Sb, as shown in Fig. 15b. The driving force for the nucleation of α-Sb exceeds that of β-Li_2Sb already at overpotentials as small as 0.03 eV. The insertion of Li into α-Sb, therefore, results in comparable driving forces for β-Li_2Sb and γ-Li_3Sb at all but the smallest overpotentials while the extraction of Li from γ-Li_3Sb very quickly produces much larger driving forces for the nucleation of α-Sb than for β-Li_2Sb.

The thermodynamic and kinetic properties calculated in this work along with the NMR observations suggest that much higher overpotentials are accessible in γ-Li_3Sb than in α-Sb. Li is remarkably mobile in γ-Li_3Sb, with migration barriers predicted between 0.1 to 0.13 eV. These migration barriers are lower even than those encountered in intercalation compounds.[34,49–51] Furthermore, the calculated free energy of off-stoichiometric γ-Li_3Sb indicates that this phase can very easily tolerate a high concentration of vacancies. The metastable part of the calculated voltage profile of γ-Li_3Sb (Fig. 7) shows that overpotentials of $\sim$ 0.2 are easily achievable through the introduction of Li vacancies. Li can therefore be extracted very rapidly from γ-Li_3Sb and in large numbers, resulting in high overpotentials. This is supported by the *in situ* NMR measurements, which show that Li extraction from γ-Li_3Sb results in large off-stoichiometry. The predicted Li mobility at dilute concentrations within the A7 crystal structure of Sb, in contrast, is very low, with migration barriers around 0.7 eV and above. Reaching large underpotentials due to the insertion of Li in excess of the solubility limit of α-Sb (with respect to β-Li_2Sb formation) will not occur rapidly as a result of sluggish Li mobility.

As with path hysteresis in $CuTi_2S_4$, a model displacement reaction analyzed using a first-principles multi-scale approach,[19] path hysteresis in the Li-Sb alloying reaction arises from a very high Li diffusion coefficient in the fully lithiated phase. The kinetic ease of extracting Li from the fully lithiated phase renders a metastable path kinetically more accessible than the true equilibrium path. The lever effect on the nucleation driving forces then likely leads to the nucleation of α-Sb rather than the thermodynamically more stable intermediate β-Li_2Sb phase. In the Li-Sb system, path hysteresis upon charge (i.e. Li extraction) should be avoidable if Li extraction occurs sufficiently slowly in a voltage window where a driving force to nucleate β-Li_2Sb exists but where a similar driving force to nucleate α-Sb is not present. Nevertheless, path hysteresis may be difficult to suppress using realistic charge rates, since β-Li_2Sb is thermodynamically stable in only a very small voltage window and the Li mobility in Li_3Sb is exceptionally high.

Journal of Materials Chemistry A Accepted Manuscript

5 Conclusion

The aim of this work was to identify the origins of phase transformation hysteresis during the electrochemical cycling of Sb electrodes in Li-ion batteries. The phases that form during the electrochemical reaction of Li with Sb electrodes (α-Sb, β-Li_2Sb and γ-Li_3Sb) are crystallographically very similar. While β-Li_2Sb and γ-Li_3Sb are line compounds in the Li-Sb phase diagram, our first-principles statistical mechanical analysis suggests that they can tolerate high concentrations of Li vacancies without incurring a large free energy penalty. Calculations of Li migration barriers predict that Li has a very low mobility in α-Sb, having to overcome migration barriers of the order of 0.7 eV. Li is, however, predicted to be remarkably mobile in γ-Li_3Sb and β-Li_2Sb with migration barriers between 0.15 and 0.25 eV. Mobility is seen experimentally for non-stoichiometric γ-Li_3Sb. An analysis of nucleation driving forces reveals a large lever effect upon Li removal from γ-Li_3Sb, with the nucleation driving force for α-Sb exceeding that for β-Li_2Sb already at small overpotentials. This, together with a very high Li mobility in γ-Li_3Sb, which facilitates large overpotentials, provides an explanation for the phase transformation hysteresis observed when cycling Sb electrodes. NMR experiments are in agreement with these proposals, β-Li_2Sb and γ-Li_3Sb being observed on discharge, charge occurring first via the delithiation of γ-Li_3Sb and then the transformation of $Li_{3-\zeta}Sb$ to Sb. The results show that non-stoichiometry of the alloy phases coupled with rapid Li transport can play a critical role in controlling the structural pathways taken by electrode materials on charge.

The triggers of phase transformation hysteresis identified here for the Li-Sb alloying reaction are likely also prevalent in intercalation compounds and other alloying reactions that suffer from path hysteresis. While high cation mobilities are usually desirable, especially when the equilibrium path passes through a solid solution, it may lead to path hysteresis when kinetically more sluggish phase transformations must also occur. The overpotentials that arise when the electrode passes through a metastable solid solution can lead to thermodynamic driving forces to transform to phases having a larger change in Li concentration than intermediate phases along the equilibrium path. This will be more likely in systems where intermediate phases are only globally stable in a narrow voltage window, as is the case for Li_2Sb in the Li-Sb system. These principles suggest that the suppression of path hysteresis requires a careful balance among all competing kinetic processes during Li insertion and removal, especially between the rates of Li diffusion and phase transformations.

Acknowledgement

This work was supported by the NorthEast Center for Chemical Energy Storage, an Energy Frontier Research Center funded by the U.S Department of Energy, and the Office of Basic Energy Science under award No. DE-SC0012583 (DC, CPG, AVDV). HH, KEJ, MM, LM and CPG thank the Alistore ERI for funding. The first-principles calculations were performed using computational resources provided by the National Energy Research Scientific Computing Center (NERSC), supported by the Office of Science and U.S. Department of Energy, under Contract Number DE-AC02-05CH11231. We thank Cyril Marino for preparing the electrodes used in the NMR study and for helpful discussion. Images of crystal structures were produced with VESTA.[57]

References

1 M. S. Whittingham, *Chem. Rev.*, 2004, **104**, 4271–4302.
2 J. Tarascon and M. Armand, *Nature*, 2001, **414**, 359–367.
3 N. Yabuuchi, K. Kubota, M. Dahbi and S. Komaba, *Chem. Rev.*, 2014, **114**, 11636–11682.
4 V. Palomares, P. Serras, I. Villaluenga, K. B. Hueso, J. Carretero-Gonzalez and T. Rojo, *Energy Environ. Sci.*, 2012, **5**, 5884–5901.
5 P. Poizot, S. Laruelle, S. Grugeon, L. Dupont and J. Tarascon, *Nature*, 2000, **407**, 496–499.
6 M. Thackeray, J. Vaughey, C. Johnson, A. Kropf, R. Benedek, L. Fransson and K. Edstrom, *J. Power Sources*, 2003, **113**, 124–130.
7 M. Morcrette, P. Rozier, L. Dupont, E. Mugnier, L. Sannier, J. Galy and J. Tarascon, *Nat. Mater.*, 2003, **2**, 755–761.
8 J. Cabana, L. Monconduit, D. Larcher and M. Rosa Palacin, *Adv. Mater.*, 2010, **22**, E170–E192.
9 P. G. Bruce, S. A. Freunberger, L. J. Hardwick and J.-M. Tarascon, *Nat. Mater.*, 2012, **11**, 19–29.
10 Y.-C. Lu, B. M. Gallant, D. G. Kwabi, J. R. Harding, R. R. Mitchell, M. S. Whittingham and Y. Shao-Horn, *Energy Environ. Sci.*, 2013, **6**, 750–768.
11 Girishkumar, G.; McCloskey, B.; Luntz, A. C.; Swanson, S.; Wilcke, W., *J. Phys.Chem. Lett.*, 2010, **1**, 2193–2203.
12 S. Evers and L. F. Nazar, *Acc. Chem. Res.*, 2013, **46**, 1135–1143.
13 T. Hatchard and J. Dahn, *J. Electrochem. Soc.*, 2004, **151**, A838–A842.
14 M. Winter and J. O. Besenhard, *Electrochim. Acta.*, 1999, **45**, 31 – 50.
15 R. A. Huggins, *J. Power Sources*, 1999, **81**, 13 – 19.
16 P. G. Bruce, B. Scrosati and J.-M. Tarascon, *Angewandte Chemie International Edition*, 2008, **47**, 2930–2946.
17 M. Obrovac and L. Christensen, *Electrochem. Solid-State Lett.*, 2004, **7**, A93–A96.
18 R. E. Doe, K. A. Persson, Y. S. Meng and G. Ceder, *Chem. Mater.*, 2008, **20**, 5274–5283.
19 H.-C. Yu, C. Ling, J. Bhattacharya, J. C. Thomas, K. Thornton and A. Van der Ven, *Energy Environ. Sci.*, 2014, **7**, 1760–1768.
20 B. Key, M. Morcrette, J.-M. Tarascon and C. P. Grey, *J. Am. Chem. Soc.*, 2011, **133**, 503–512.
21 A. Van der Ven, K. Garikipati, S. Kim and M. Wagemaker, *J. Electrochem. Soc.*, 2009, **156**, A949–A957.
22 A. Mukhopadhyay and B. W. Sheldon, *Prog. Mater. Sci.*, 2014, **63**, 58–116.
23 C.-M. Park, S. Yoon, S.-I. Lee, J.-H. Kim, J.-H. Jung and H.-J. Sohn, *J. Electrochem. Soc.*, 2007, **154**, A917–A920.
24 K. Hewitt, L. Beaulieu and J. Dahn, *J. Electrochem. Soc.*, 2001, **148**, A402–A410.
25 L. Baggetto, P. Ganesh, C.-N. Sun, R. A. Meisner, T. A. Zawodzinski and G. M. Veith, *J. Mater. Chem. A*, 2013, **1**, 7985–7994.
26 C.-M. Park, J.-H. Kim, H. Kim and H.-J. Sohn, *Chem. Soc. Rev.*, 2010, **39**, 3115–3141.
27 J. P. Perdew, K. Burke and M. Ernzerhof, *Phys. Rev. Lett.*, 1996, **77**, 3865–3868.
28 G. Kresse and J. Furthmüller, *Phys. Rev. B*, 1996, **54**, 11169–11186.
29 G. Kresse and J. FurthmÃijller, *Comput. Mater. Sci.*, 1996, **6**, 15 – 50.
30 G. Kresse and D. Joubert, *Phys. Rev. B*, 1999, **59**, 1758–1775.
31 P. E. Blöchl, *Phys. Rev. B*, 1994, **50**, 17953–17979.
32 J. Sanchez, F. Ducastelle and D. Gratias, *Physica A*, 1984, **128**, 334–350.
33 D. deFontaine, in *Solid. State. Phys.*, ed. Ehrenreich, H and Turnbull, D, Academic Press, 1994, vol. 47, pp. 33–176.
34 A. Van der Ven, J. C. Thomas, Q. Xu, B. Swoboda and D. Morgan, *Phys. Rev. B*, 2008, **78**, 104306.
35 A. Van der Ven, J. C. Thomas, Q. Xu and J. Bhattacharya, *Math. Comput. Simul.*, 2010, **80**, 1393–1410.
36 B. Puchala and A. Van der Ven, *Phys. Rev. B*, 2013, **88**, 094108.
37 G. Henkelman and H. Jonsson, *J. Chem. Phys.*, 2000, **113**, 9978–9985.
38 A. V. Krukau, O. A. Vydrov, A. F. Izmaylov and G. E. Scuseria, *J. Chem. Phys.*, 2006, **125**, 224160.
39 B. Key, R. Bhattacharyya, M. Morcrette, V. Seznec, J.-M. Tarascon and C. P. Grey, *J. Am. Chem. Soc.*, 2009, **131**, 9239–9249.
40 J. Sangster and A. Pelton, *J. Phase Equilib.*, 1993, **14**, 514–517.
41 W. Muller, *Z. Naturforsch. B.*, 1977, **32**, 357–359.
42 G. Brauer and F. Zintl, *Z. Phys. Chem. B-Chem. E.*, 1937, **37**, 323–352.
43 M. SaubanÃÍre, M. B. Yahia, F. Lemoigno and M.-L. Doublet, *J. Power Sources*, 2015, **280**, 695 – 702.
44 B. S. Hickman, *J. Mater. Sci*, 1969, **4**, 554–563.
45 M. Usikov and Zilbershtein.VA, *Phys. Status Solidi A*, 1973, **19**, 53–58.
46 A. G. KhachaturiÍąan, *Theory of structural transformations in solids*, Wiley, New York, 1983.
47 A. S. Dalton, A. A. Belak and A. Van der Ven, *Chem. Mater.*, 2012, **24**, 1568–

Journal of Materials Chemistry A Accepted Manuscript

This journal is © The Royal Society of Chemistry [year]

1574.
48 A. Van der Ven, J. Bhattacharya and A. A. Belak, *Acc. Chem. Res.*, 2013, **46**, 1216–1225.
49 A. Van der Ven, G. Ceder, M. Asta and P. D. Tepesch, *Phys. Rev. B*, 2001, **64**, 184307.
50 J. Bhattacharya and A. Van der Ven, *Phys. Rev. B*, 2010, **81**, 104304.
51 J. Bhattacharya and A. Van der Ven, *Phys. Rev. B*, 2011, **83**, 144302.
52 G. H. Vineyard, *J. Phys. Chem. Solids*, 1957, **3**, 121–127.
53 S. Chaudhuri, F. Wang and C. Grey, *J. Amer. Chem. Soc.*, 2002, **124**, 11746–11757.
54 B. Key, R. Bhattacharyya, M. Morcrette, V. Seznec, J.-M. Tarascon and C. P. Grey, *J. Am.Chem.Soc.*, 2009, **131**, 9239–9249.
55 H. Jung, P. K. Allan, Y.-Y. Hu, O. J. Borkiewicz, X.-L. Wang, W.-Q. Han, L.-S. Du, C. J. Pickard, P. J. Chupas, K. W. Chapman, A. J. Morris and C. P. Grey, *Chem. Mater.*, 2015, **27**, 1031–1041.
56 R. W. Balluffi, S. M. Allen and W. C. Carter, *Nucleation*, John Wiley and Sons, Inc., 2005, pp. 459–499.
57 K. Momma and F. Izumi, *J.Appl.Crystallogr.*, 2008, **41**, 653–658.

Journal of Materials Chemistry A Accepted Manuscript